International Journal of Refractory Metals and Hard Materials 112 (2023) 106152

Contents lists available at ScienceDirect

International Journal of Refractory Metals and Hard Materials

journal homepage: www.elsevier.com/locate/IJRMHM

Micro-nano secondary phase greatly increases the plasticity of titanium-zirconium-molybdenum alloy

Shi-Lei Li [a,b], Ping Hu [a,b,*], Tong Liu [a,b], Qian-Shuang Shi [a,b], Bo-Liang Hu [a,b], Xing-Jiang Hua [a,b], Song-Wei Ge [a,b], Jia-Yu Han [a,b], Wen Zhang [c,**], Kuai-She Wang [a,b], Alex A. Volinsky [d]

[a] *School of Metallurgy Engineering, Xi'an University of Architecture and Technology, Xi'an 710055, China*
[b] *National and Local Joint Engineering Research Functional Center for Materials Processing, Xi'an University of Architecture and Technology, Xi'an 710055, China*
[c] *Northwest Institute for Non-ferrous Metal Research, Xi'an 710016, China*
[d] *Department of Mechanical Engineering, University of South Florida, 4202 E. Fowler Ave., ENG 030, Tampa, FL 33620, USA*

ARTICLE INFO

Keywords:
Titanium-zirconium-molybdenum alloy
Mechanical properties
Micro-nano-scale secondary phase
Stacking fault
Substructure

ABSTRACT

Improving ductility without sacrificing strength remains challenging for brittle molybdenum and its alloys. Titanium-zirconium-molybdenum alloy with the micro-nano-scale secondary phases (MN-TZM) was prepared using titanium sulfate, zirconium nitrate, fructose, and molybdenum powder as raw materials. The elongation at failure of the MN-TZM alloy was increased by 2.3 times to 15.1% without sacrificing strength. The fracture of the MN-TZM alloy exhibited cleavage and ductile tearing characteristics. Transmission electron microscopy and electron backscatter diffraction results indicate that dislocations can slip along the (110) plane at different strains, bypassing or even passing through the micro-nano-scale secondary phase (MN-SP) in MN-TZM alloys. The stacking faults and dislocation junctions of the MN-TZM alloy substructure avoid stress concentration and enhance the deformation ability. This study provides theoretical guidance for the industrial production of high-performance secondary-phase dispersion-strengthened structural materials, linking process-structure-properties relationships.

1. Introduction

Increasing ductility without sacrificing strength has been a key goal for traditional engineered structural materials used in various critical applications. To this objective, researchers have adopted a variety of strategies, such as the formation of nanometer twins [1,2], a dispersed secondary phase [3,4], atomic clusters [5,6], gradient structures [7,8], other structures [9], metastable structures, and bimodal/multimodal grain structures in the matrix. Introducing a dispersed secondary phase into the alloy has attracted much attention due to its universal applicability in many alloy systems [10–12]. It is expected to pin and accumulate many dislocations, thereby increasing the strain hardening rate and the plastic deformation ability of the alloy [12,13]. In addition, the interaction between dislocations and uniformly distributed secondary phases (Orowan rings or particle shearing) can also enhance the matrix properties [14]. For molybdenum (Mo), the high-temperature mechanical properties and high-temperature microstructure stability due to dispersed secondary phase expand its applications [15]. Despite molybdenum alloys' high strength and hardening levels, their ductility is limited at medium or low temperatures. Commercial Mo alloys suitable for mass production typically have a uniform elongation of only a few percent before fracture. Insufficient ductility is a well-known performance flaw restricting its engineering applications [16]. For example, poor ductility and radiation-induced embrittlement are significant problems in the nuclear field [17–19].

Improving the ductility of Mo alloys near room temperature has been an important research goal in recent decades. Researchers often choose complicated Mo alloy systems [20] or are keen on processes with tiny yields and long processing cycles [12]. For example, improving the plastic flow properties of Mo by adding rhenium (Re) as a solute element effectively promotes dislocation motion, but this approach leads to softening and is costly due to expensive Re [21]. Adding a small amount of oxide or carbide particles to Mo acting as grain refiners results in smaller grain sizes than unalloyed products. For example, the grains of Mo alloys can be refined by adding Al_2O_3 [22–24]. The ductility of the specimen can be improved by adding spinel ($MgAl_2O_4$) to the Mo matrix

---

* Corresponding author at: School of Metallurgy Engineering, Xi'an University of Architecture and Technology, Xi'an 710055, China.
** Corresponding author.
E-mail addresses: huping@xauat.edu.cn (P. Hu), gwenzh@163.com (W. Zhang).

https://doi.org/10.1016/j.ijrmhm.2023.106152
Received 14 November 2022; Received in revised form 3 February 2023; Accepted 11 February 2023

[25]. Adding La_2O_3 or other rare earth oxides to Mo can increase its recrystallization temperature, purify grain boundaries, and improve its mechanical properties [26–28]. The addition of carbides to these alloys is less studied, mainly limited to TiC additives. Adding nano-titanium carbide to titanium-zirconium-molybdenum (TZM) alloys supplemented by field-assisted sintering technology can refine grains and increase hardness [29].

However, the above studies focus on improving the properties of Mo alloys using one or several additives that are not commonly used in industrial production or employing cumbersome preparation processes that are not suitable for mass production. The researchers did not address the room temperature brittleness of Mo alloys, which are widely used in engineering applications. This research is based on the TZM alloy (0.4–0.8 wt% Ti, 0.06–0.12 wt% Zr, 0.01–0.04 wt% C), one of the most widely used Mo alloys in the industry. This study prepared a TZM alloy (abbreviated as MN-TZM alloy) with a micro-nano-scale secondary phase (MN-SP). The control group is a conventional micron-scale secondary phase (M-SP) TZM alloy (referred to as the TZM alloy). Compared with the TZM alloy, the MN-TZM alloy has a smaller grain size and more uniform secondary phase distribution, and its room temperature elongation is 2.3 times higher than conventional TZM. This doping method to prepare dispersion-strengthened alloys using solutions instead of powders can be used for other dispersion-strengthened alloy systems and is suitable for industrial production.

2. Experiment procedure

The melting point of refractory Mo metal is 2610 °C, and powder metallurgy is usually used to prepare Mo alloys. Powder metallurgy is a technology that uses metal powder or a mixture of metal and non-metal powders as raw materials to manufacture metals, composite materials, and various products. The raw materials used for preparing MN-TZM alloy include titanium sulfate (~0.6 wt% Ti), zirconium nitrate (~0.1 wt% Zr), organic carbon source fructose (~0.04 wt% C), and high-purity Mo powder. The high-purity Mo powder used in the experiment has a purity $\geq$ of 99.95%, a particle size of $\leq$7 μm, and the grade is FMo-1. Titanium sulfate and zirconium nitrate were both white powders with particle sizes of $\leq$13 μm. The alloy composition of the MN-TZM alloy powders is shown in Table 1. The doping raw materials were mixed with a solution of deionized water and anhydrous ethanol, mixed with Mo powder by solid-liquid doping, and stirred by hand for 15 min. The weight ratio of deionized water and anhydrous ethanol solutions for mixing MN-TZM powders was 1:1. The mixture was dried in a DZ-2BCIV vacuum oven at 100 °C for 1 h to evaporate excess water. After drying, the mixed alloy powder was placed in a quartz tube filled with 99.99% hydrogen and was reduced in an SK2–8-17TPD3 tube furnace at 700 °C for two hours and then cooled to room temperature with the furnace. The purpose was to remove the impurity elements S, N, and O from the mixed alloy powder. TZM alloy raw materials include titanium hydride (~0.6 wt% Ti), zirconium hydride (~0.1 wt% Zr), and fructose (~0.04 wt% C). The TiH_2 powder and ZrH_2 powder used in the experiment were both black-gray powders with particle sizes of $\leq$25 μm, and the grades are THP20–1 and FZH-1, respectively. The alloy composition of the TZM alloy is shown in Table 1. The alloy powder was placed into a nitrogen-filled plastic bottle and mixed in an SYH three-dimensional mixer for 100 min.

To ensure the fluidity of the alloy powder and improve the uniformity of mixing, the above two alloy powders were ball-milled in a PMQW4L planetary ball mill at 40 rpm for 2 h; the balls-to-material ratio was 2:1, and the Mo ball diameter was 4–10 mm. After ball milling, the alloy powder was filled into a custom-made rubber grinding tool, and the LDJ2150/3000-250YS cold isostatic press was used for compression molding at 180 MPa pressure applied for 10 min. The compact was placed in an HM3002 medium frequency induction sintering furnace filled with 99.99% hydrogen for sintering and densification. The sintering process is shown in Fig. 1. Mo alloy powder undergoes a series of physical and chemical changes during the sintering process: evaporation of moisture or volatile organic substances, removal of adsorbed gases, stress relief, reduction of surface oxide powder particles, mass transfer between particles, and grain growth [30]. Therefore, the process is divided into 4 stages to ensure that each process is completed in a hydrogen furnace. The thickness of the sintered billet is 12 mm, and the rolling process includes hot rolling and cold rolling: hot rolling at 1300 °C, from 15.6 mm to 3.9 mm (annealing at 850 °C); warm rolling at 600 °C, from 3.9 mm to 1.3 mm (annealing at 850 °C and alkali washing); cold rolling at 400 °C, from 1.3 mm to 0.5 mm. The shape and size of the tensile test sample is shown in Fig. 2a. To remove internal stress in the alloy, the rolled plates were annealed under argon protection at 950 °C for 2 h. The non-reducing gas of argon cannot remove the oxide scale on the surface of the alloy, so it causes very slight oxidation on the surface of the tensile sample, which does not affect the mechanical property test.The elongation at failure and ultimate tensile strength of the two alloy sheets were obtained using the Instron8801 electro-hydraulic servo testing machine, and three repetitions were performed. To observe the deformed structure of the alloy at different strains, the elongation at failure was divided into 5 equal parts, and 5 samples were tested to different maximum strains. After determining the maximum strain at failure, other samples were tested at lower strain levels to characterize their deformed structure, as shown in Fig. 2. The samples were painted with white paint for better contrast needed for strain measurements. All tests were performed in air at room temperature.The samples prepared for SEM detection were hand-polished and wiped against the surface using a corrosive solution (NaOH: $K_3[Fe(CN)_6]$: H_2O = 1: 1: 10 wt%). The samples prepared for EBSD detection were hand-polished and corroded by electrolysis in a specific electrolyte (H_2SO_4: CH_3CH_2OH: H_2O = 1: 2: 5 wt%) at the voltage of 12 V for 80 s. Samples prepared for TEM detection were hand-ground to 30–50 μm and then thinned through the double-jet electrolytic thinning instrument.

A Gemini SEM 300 field emission scanning electron microscope equipped with an electron backscatter diffraction (EBSD) and energy dispersive X-ray spectroscopy (EDS) systems were used to observe the microstructure of the alloy and to analyze the secondary phase composition. EBSD data acquisition time is 40 min per sample, and the

Table 1
Composition design of TZM alloy (g).

	Fructose	$Ti(SO_4)_2$	$Zr(NO_3)_4$	TiH_2	ZrH_2	Mo
MN-TZM	1	30	3.73	–	–	1000
TZM	1	–	–	6.25	1.02	1000

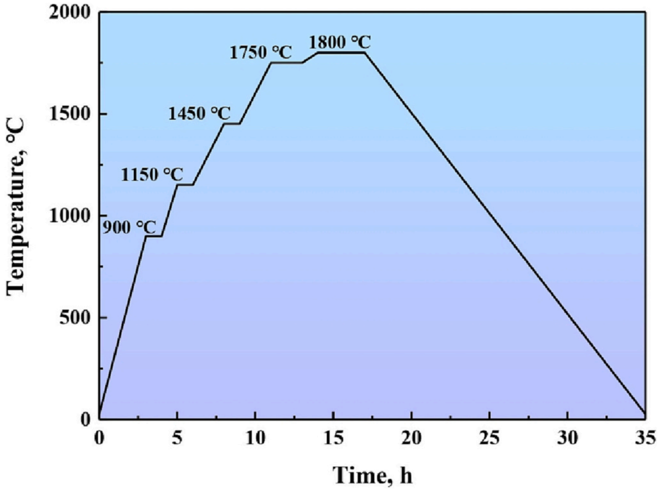

Fig. 1. Mo alloy sintering process.

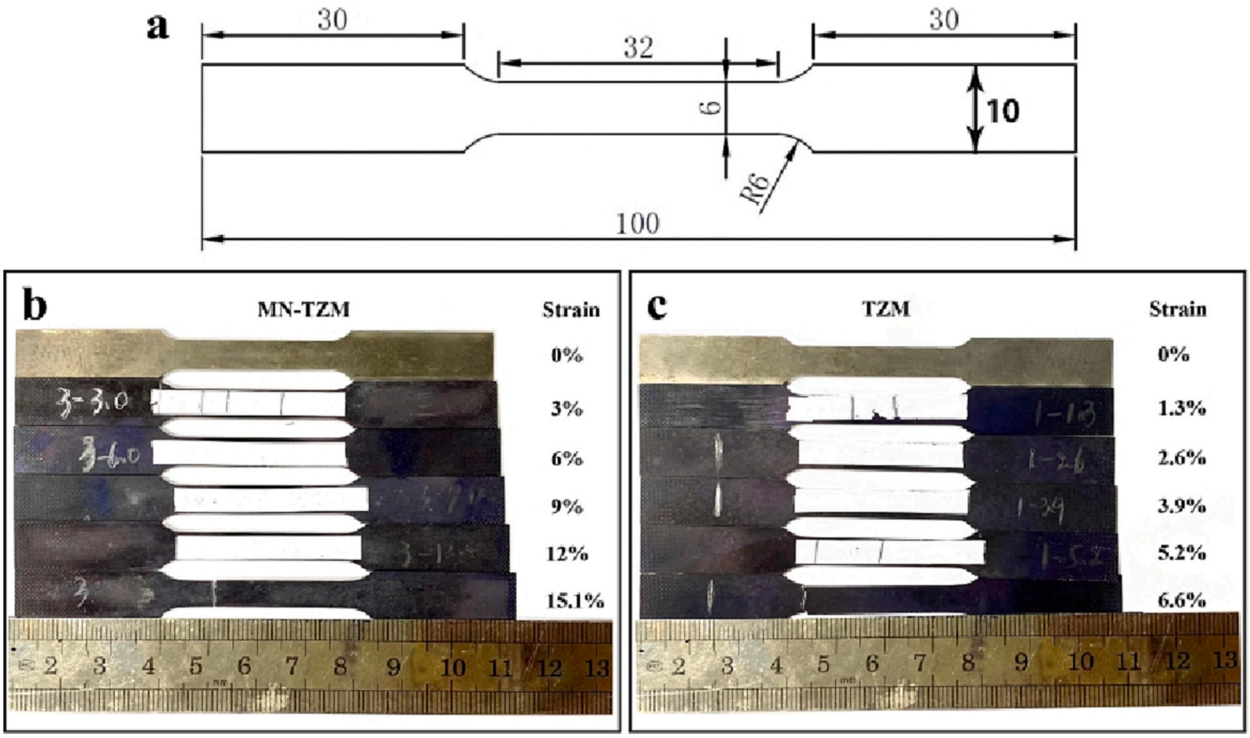

Fig. 2. Tensile samples of the Mo alloys subjected to different maximum strain: (a) shape and size of the tensile test sample (mm), (b) MN-TZM alloy, (c) TZM alloy.

data were analyzed using the Channel 5 software. The microstructure features of the alloy were observed by the Talos F200X field emission transmission electron microscope. The average grain size of the Mo alloy sintered samples was measured by the intercept method. The average grain size of rolled and tensile sheets was calculated through Channel 5 software.After the material is violently deformed, the misorientation angle in each part of the grain is very large. Annealing reduces the misorientation angle in tiny areas inside the grain. If the misorientation of each adjacent micro-region in the grain is large, it is deformed grain. If micro-regions with large misorientation and micro-regions with small misorientation coexist in the grain, it is substructured (subgrains). If there is almost no misorientation between each adjacent micro-region inside the entire grain, it is recrystallized grain. Specifically, in the Channel 5 software, grains with an average misorientation >7.5 are identified as deformed grains, >1 < 7.5 are identified as substructured, and <1 are identified as recrystallized grains.

3. Results and discussion

3.1. Microstructure analysis

Fig. 3 shows the typical microstructure of the MN-TZM and TZM alloys, including sintered billets and rolled sheets. As seen in Fig. 3a, b, the microstructure of the sintered billets of both alloys contains equiaxed crystals, a secondary phase of oxide particles, and pores. The microstructure of the rolled sheets of the two alloys contains broken grains and secondary phases. The secondary phases in the MN-TZM alloy are uniformly distributed in the matrix, while the large-scale secondary phases in the TZM alloy tend to be distributed at grain boundaries. From the EDS results, the secondary phase of the two alloys is mainly oxides. It is worth noting that the M-SP in the TZM alloy was cracked during rolling (Fig. 3d), which did not occur in the MN-TZM alloy (Fig. 3c). The brittle oxide secondary phase is difficult to deform with the plastic deformation of the alloy, and for the MN-SP it is easier to maintain its original shape due to its smaller stress area. As seen in Fig. 3, the average secondary phase particle size of the MN-TZM alloy sintered billet is 900 ± 91 nm, and the average grain size is 18.0 ± 4.8 μm, while for the TZM alloy the corresponding values are 2.4 ± 8.3 μm and 25.6 ± 3.6 μm. The size of the secondary phase particles of the MN-TZM alloy rolled sheet is further reduced to 740 ± 42 nm, while the secondary phase particles' size of the TZM alloy rolled sheet is 2.4 ± 6.7 μm. The average grain size of the MN-TZM alloy is reduced by 29.7% compared with the TZM alloy. This indicates that the hindering effect of MN-SP on grain growth of the TZM alloy is more evident than the M-SP. The XRD patterns are shown in Fig. 3e, f. Only the characteristic peaks of Mo have been found. The XRD method cannot detect a phase with a content of <1%, and the amount of each element added in both molybdenum alloys was <1%, so they cannot be identified.

3.2. MN-SP hinders the growth of Mo alloy grains

Fig. 4 is a schematic diagram illustrating the hindering effect of the secondary phase particles on grain boundary migration. Let's assume that the secondary phase is spherical with radius r, and assume that the grain boundary has shifted to the right from the position shown in Fig. 4a to the position shown in Fig. 4b. Due to the pinning effect of the secondary phase particles, the part of the grain boundary in contact with the secondary phase particles lags behind other parts. The leftward force F in N exerted by the secondary phase on the grain boundary is the reason why the migration of the grain boundary is hindered. If equilibrium is reached in the state shown in Fig. 4, the magnitude of this force F must be equal to the horizontal component of the total interface tension. As shown in Fig. 5b, σ is the interfacial tension in N/m, the perimeter length of the grain boundary in contact with the particle is $2\pi r \cos \varnothing$, the total tension is $2\pi r \cos \varnothing \sigma$, and its component force in the horizontal direction should be multiplied by $sin\beta$. $\beta = 90^\circ + \varnothing - \alpha$, so $sin\beta = cos(90^\circ - \beta) = cos(\alpha - \varnothing)$, the equilibrium condition should be [31–33]:

$$F = 2\pi r cos\varnothing\sigma cos(\alpha - \varnothing) \quad (1)$$

However, ∅ varies with the relative position of the grain boundary and the secondary phase. The contact angle α depends only on the

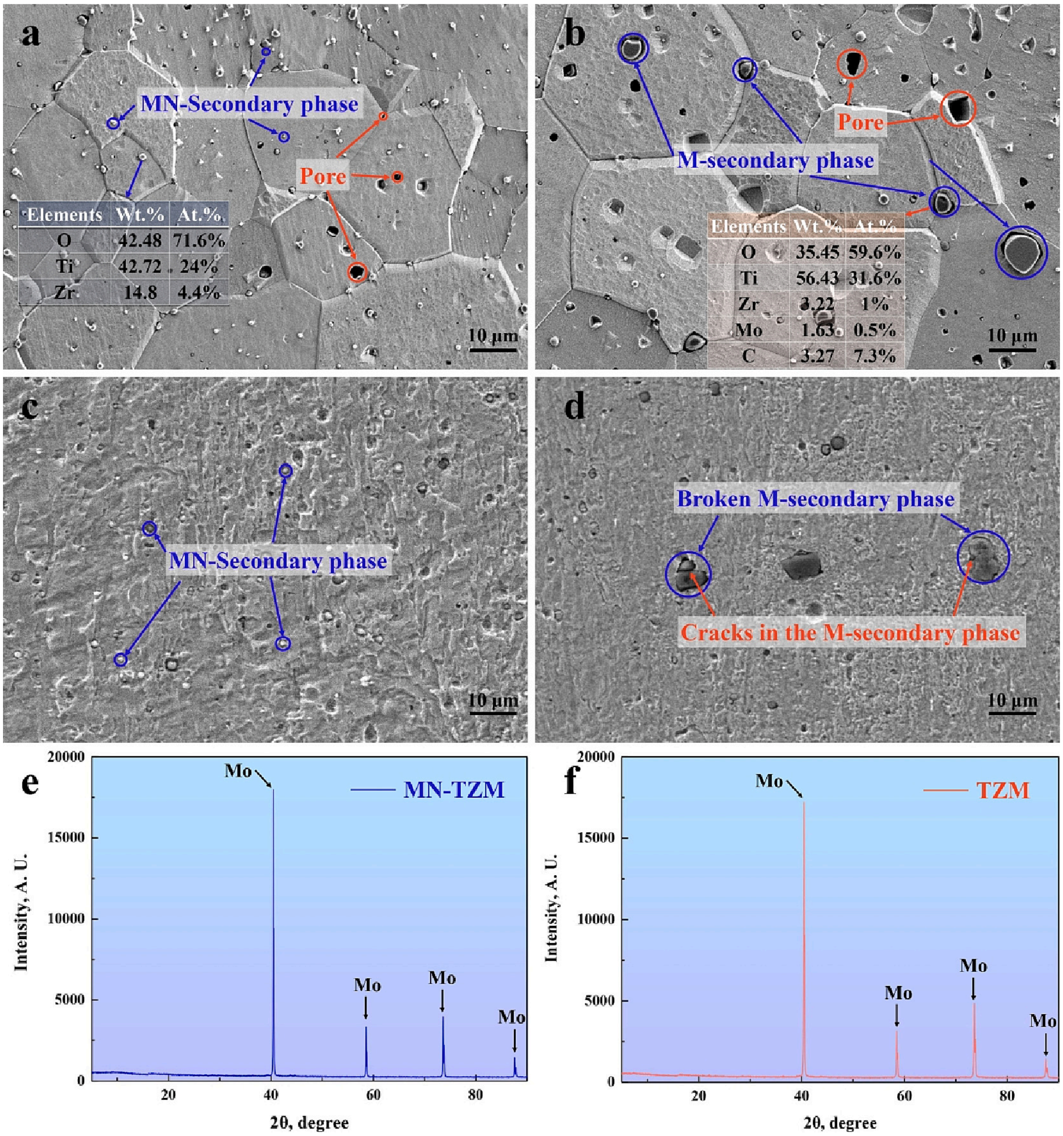

Elements	Wt.%	At.%
O	42.48	71.6%
Ti	42.72	24%
Zr	14.8	4.4%

Elements	Wt.%	At.%
O	35.45	59.6%
Ti	56.43	31.6%
Zr	3.22	1%
Mo	1.63	0.5%
C	3.27	7.3%

Fig. 3. SEM images of the Mo alloys microstructure: (a) MN-TZM alloy sintered sheet, (b) TZM alloy sintered sheet, (c) MN-TZM alloy rolled sheet, (d) TZM alloy rolled sheet, (e) XRD patterns of MN-TZM alloy, and (f) XRD patterns of TZM alloy.

interfacial energy between the secondary phase and the grains and has a constant value that depends on the properties of the secondary phase. If $\varnothing$ takes the maximum value, let $\mathrm{d}f/\mathrm{d}\varnothing = 0$, then $\varnothing = \alpha/2$, combined with the eq. (1), the maximum value F_{max} of the force between the secondary phase particle and the grain boundary can be obtained as in [31–33]:

$$F_{max} = \pi r\sigma(1 + cos\alpha) \tag{2}$$

If there is only one secondary phase particle, then the maximum resistance to grain boundary movement should mainly depend on the particle size r, based on Eq. (2). However, for the whole structure, the average speed of grain growth is w3not only related to the secondary phase size but also closely related to the number of secondary phase particles per unit volume in the metal structure. If the total volume occupied by the secondary phase is fixed, the smaller the secondary phase particle size, the greater the number of particles. The relationship between the limit size d of grain growth and the volume fraction f and the radius r of the secondary phase is [31–33]:

$$d = \frac{4}{3}\frac{r}{f(1 + cos\alpha)} \tag{3}$$

When the volume fraction f of the secondary phase in the alloy is constant, the smaller the radius r of the secondary phase, the smaller the grain size d of the alloy. When the radius of the secondary phase is constant, the larger the volume fraction of the secondary phase in the alloy, the smaller the grain size of the alloy.

Previous research showed that the secondary phase appeared from 775 °C in the TZM alloy [20,34]. Therefore, the secondary phase in the alloy hinders the growth of grains during sintering. The volume fractions of alloying elements in the two Mo alloys studied in this paper are the same. Compared with the TZM alloy, the secondary phase particles of the MN-TZM alloy are finer, more uniformly distributed, and more numerous. The MN-SP uniformly distributed in the aggregates have a strong hindering effect on grain growth. The M-SP in the TZM alloy is more distributed in the grain boundary and has a less hindering effect on bulk diffusion. This is consistent with the conclusions of the literature report [12].

Fig. 5 shows the EBSD analysis of two types of Mo rolled sheets after annealing. In Fig. 5a and e almost all deformed grains are elongated along the rolling direction, with the average grain size of 1.43 ± 5.4 μm for the MN-TZM alloy and 1.89 ± 8.7 μm for the TZM alloy. Recrystallization is the process experienced when a deformed structure develops

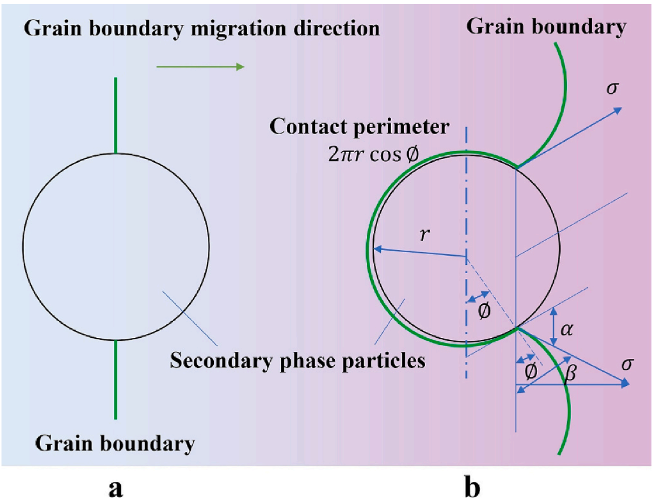

Fig. 4. Schematic diagram of the hindering effect of the secondary phase particles on grain boundary migration: (a) The relative position of the secondary phase and the grain boundary before migration, (b) grain boundary migration is hindered by the secondary phase. Adapted from reference [31].

into a new grain structure through nucleation and motion of high-angle boundaries driven by stored deformation energy [35]. Partially recrystallized grains were observed in the rolled and annealed sheets of both alloys (black circled area in Fig. 5a, e), and their proportions were 21.1% for the MN-TZM alloy and 37.3% for the TZM alloy, respectively (Fig. 5d, h). Recrystallized grains appeared in both alloys after annealing at 950 °C, indicating that the rolling process left high internal stress in both alloys. Compared with TZM alloys, MN-TZM alloys have fewer recrystallized regions because the uniformly distributed MN-SP hinders grain boundary migration during recrystallization more significantly than M-SP.

The driving force for the recrystallization of metals is the distortion energy stored in the matrix after deformation, and the resistance is the grain boundary energy. The recrystallized core can be the original high-angle grain boundary, the high-angle sub-grain boundary formed gradually by the growth of the sub-grain, and the high-angle sub-grain boundary already existed in the deformed aggregate. The recrystallization temperature of metals is the minimum temperature at which recrystallization can be completed within a specified time, or the recrystallization reaches a specified degree (such as 95%). Compared with the TZM alloy, the secondary phase particles of the MN-TZM alloy are finer, more uniformly distributed, and more numerous. Therefore, the barrier of the MN-SP to grain boundary migration is more substantial in the MN-TZM alloy, which makes the grain size of the MN-TZM alloy after annealing smaller than the TZM alloy. More deformed regions in the MN-TZM alloy also provide the possibility for the subsequent substructure value-added.

3.3. *Tensile properties at room temperature*

The room temperature true stress-strain tensile curves of the studied alloys are shown in Fig. 6a. The MN-TZM alloy exhibits ultra-high plasticity of 15.1% without loss of strength, which is 2.3 times higher than the TZM alloy. The two types of Mo alloys have almost the same strain hardening rate, while the MN-TZM alloy has better ductility. Fig. 7 shows the room temperature fracture surfaces of the two types of Mo alloys. It can be seen that the macroscopic fracture of the MN-TZM alloy is an uneven surface. The dimples perpendicular to the principal stress direction contain MN-SP particles, and the transgranular fracture cleavage plane is also present. The fracture of the MN-TZM alloy exhibits the characteristics of cleavage surface and ductile tear, which is a mixture of cleavage and quasi-cleavage fracture [36].

3.4. *Fractography analysis*

Researchers [42] divide the secondary phase particles into three categories according to their diameter: large particles (d > 1 μm); medium particles (0.01 μm ≤ d ≤ 1 μm); small particles (d < 0.01 μm). For the formation of microcracks, under the same conditions, the larger secondary phase particles easily form microcracks. Even if micropores are formed around the small secondary phase particles, it is not easy to grow because the sub-plastic zone is not easy to form. Assuming that when the tensile stress cutting through the interface between the secondary phase particles and the matrix reaches the critical stress σ_c, the secondary phase particles are separated from the matrix and microscopic pores are formed. It can be deduced that the macroscopic strain ε_n used to characterize the initiation of the holes is:

$$\varepsilon_n \approx \frac{r_p}{b}\left(\frac{\sigma_c - \sigma_m}{G}\right) \tag{4}$$

Here, r_p is the particle radius of the secondary phase, b is the Burgers vector, G is the shear modulus, and σ_m is the applied mean stress. It can be seen that when other parameters remain unchanged, the smaller the particle radius r_p of the secondary phase in the matrix, the smaller the macroscopic strain ε_n of hole initiation is. Compared with TZM alloys, the studied MN-TZM alloys have average secondary phase particles with an average size d < 1 μm, making the MN-TZM alloys produce much smaller hole-initiated macroscopic strains during tension than TZM alloys. Compared with TZM alloy, MN-TZM alloy is less prone to cracks during plastic deformation.

When the applied external force is large enough, the dislocation loops move toward the MN-SP particles. Micro-voids are formed when the accumulated elastic strain is sufficient to overcome the interfacial bonding force between the MN-SP particles and the Mo matrix to form a new surface. The formation of microscopic holes significantly reduces the repulsive force received by the following dislocations so that a large number of dislocations move to the newly generated microscopic holes under the action of external force, resulting in the growth of microscopic holes. The dislocation source located initially behind the dislocation loop is reactivated due to the disappearance of the original stacking dislocation restraint, resulting in a new dislocation loop. Since dislocations can accumulate on different slip planes, microscopic holes can be formed by the movement of dislocations on one or several slip planes. The dislocations on other slip planes move toward the microscopic holes and make them grow. The microscopic holes formed inside the Mo matrix grow continuously under the action of externally applied shear stress. The cross-section of the matrix before several adjacent microscopic holes continues to shrink until they are connected and lead to fracture, eventually forming a dimple fracture morphology. Due to the high strain hardening rate of Mo, necking is difficult to occur, leading to the generation of more microscopic pores and making the dimples smaller and shallower, as seen in Fig. 7b.

It can be seen from Fig. 5, and Fig. 7 that the proportion of recrystallized grains in the TZM alloy rolled sheet after annealing reaches 37.3%, and that of the MN-TZM alloy is 21.1%. This results in an average grain size of 1.89 μm for the TZM alloy compared to only 1.43 μm for the MN-TZM alloy. From the energy point of view, the first condition for cracks due to dislocation merging is that the Frank-Read (F-R) dislocation source in the vicinity of the crack cannot be easily activated to avoid the relaxation of elastic energy. In the body-centered cubic TZM alloy, due to the inclusion of multiple slip systems, only when a large number of dislocations are suddenly generated and collapsed together, can the F-R dislocation sources near the cracks be too late to activate.

Based on the above assumptions, Cottrell [43] proposed the dislocation reaction theory. The nucleation of cracks is automatic, and the fracture of crystals depends on the growth and propagation of cracks. The calculation result is:

$$\sigma_y k_y d^{\frac{1}{2}} = \beta \gamma G \tag{5}$$

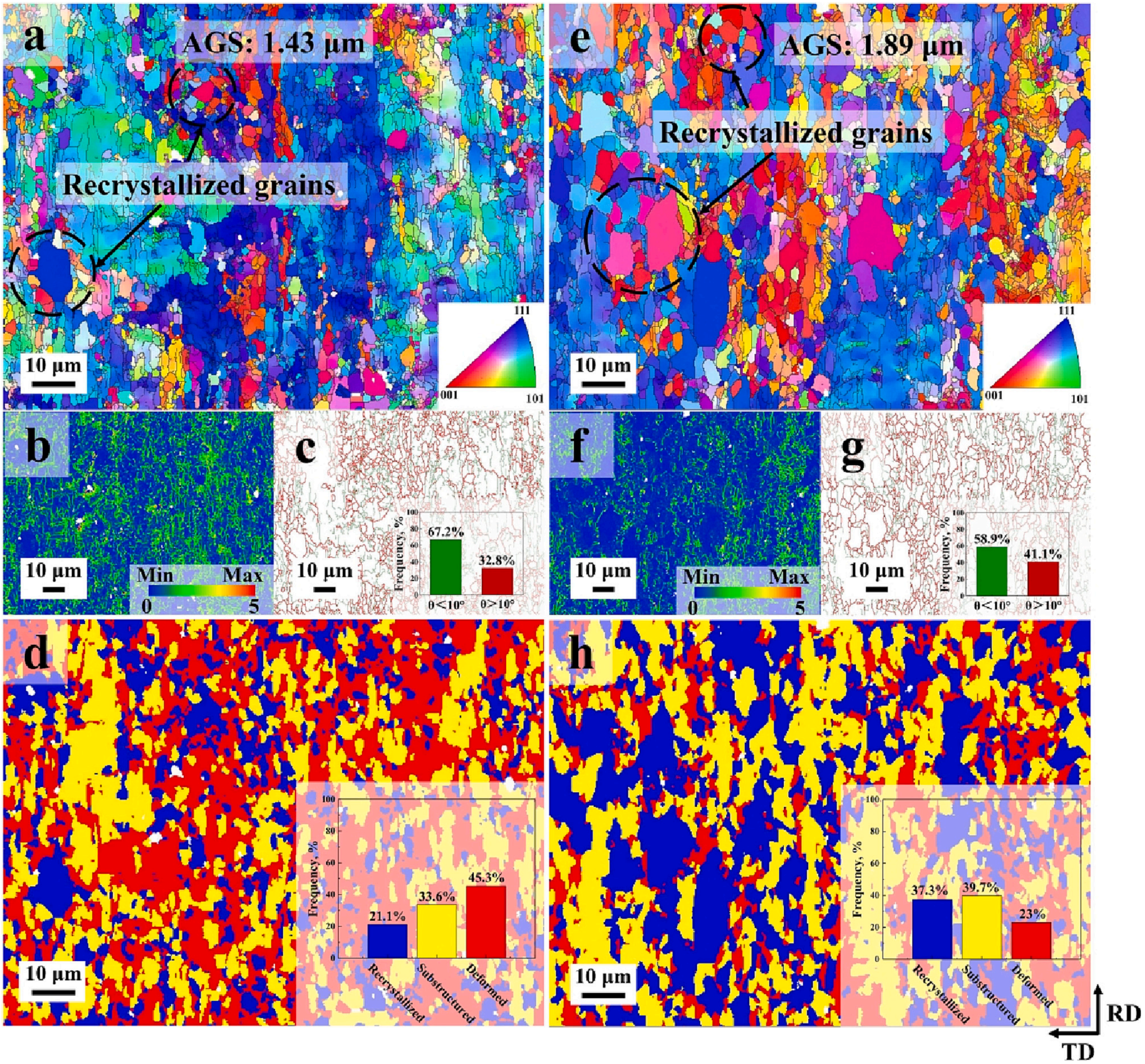

Fig. 5. EBSD analysis of annealed Mo alloy rolled sheets: (a) Inverse pole figure (IPF) diagram of the MN-TZM alloy, (b) Kernel average misorientation (KAM) diagram of the MN-TZM alloy, (c) grain boundary diagram of the MN-TZM alloy, (d) recrystallized, sub-structured, and deformed composition diagram of the MN-TZM alloy, (e) IPF diagram of the TZM alloy, (f) KAM diagram of the TZM alloy, (g) grain boundary diagram of the TZM alloy, (h) recrystallized, sub-structured, and deformed composition diagram of the TZM alloy.

Here, σ_y is the yield stress, k_y is the Hall-Petch slope, d is the grain diameter, γ is the effective surface energy, G is the shear modulus, and $\beta \approx 1$ when deformation is tensile. The condition for brittle fracture of the material is that the left side of eq. (5) is greater than the right side. Increasing the grain diameter d can lead to brittle fracture of the metal when other parameters remain unchanged. The MN-TZM alloy sheets are less prone to brittle fracture than the TZM alloy sheets because the average grain size of the annealed MN-TZM sheets is smaller than the TZM alloy sheets.

The studied Mo alloys contain secondary phase particles, in which case the deformation is hindered by the secondary phase, and the presence of the secondary phase also tends to nucleate cracks. Smith considered the effect of secondary phase particles on brittle material fracture and proposed the following model [44]:

$$\left(\frac{C_0}{d}\right)^2 \sigma_f + \tau_e\left[1+\frac{4}{\pi}\left(\frac{C_0}{d}\right)^{1/2}\frac{\tau_i}{\tau_e}\right]^2 \geq \left[\frac{4E\gamma_P}{\pi(1-v^2)d}\right]^{1/2} \tag{6}$$

Here, C_0 is the thickness of the secondary phase particle, d is the grain diameter, σ_f is the cleavage fracture stress, $\tau_e = \tau - \tau_i$, where τ is the shear stress and τ_i is the lattice resistance, E is the elastic modulus of the material, γ_P is the effective surface energy, and v is the Poisson's ratio.

Combining Eqs. (5) and (6), the critical stress for crack propagation at room temperature can be obtained from the energy balance condition. That is, the fracture stress is σ_f [44]:

$$\sigma_f = \left[\frac{8G\gamma_P}{\pi(1-v)C_0}\right]^{1/2} \tag{7}$$

Eqs. (4) and (7) introduce the structural factors of the material into the fracture process, which illustrate the influence of the thickness C_0 of the brittle secondary phase particles on the critical cleavage fracture stress. The larger the size of the secondary phase, the smaller the critical cleavage fracture stress of the material. In other words, materials containing large-scale secondary phase particles are more prone to brittle fracture. The average secondary phase particle size and average grain

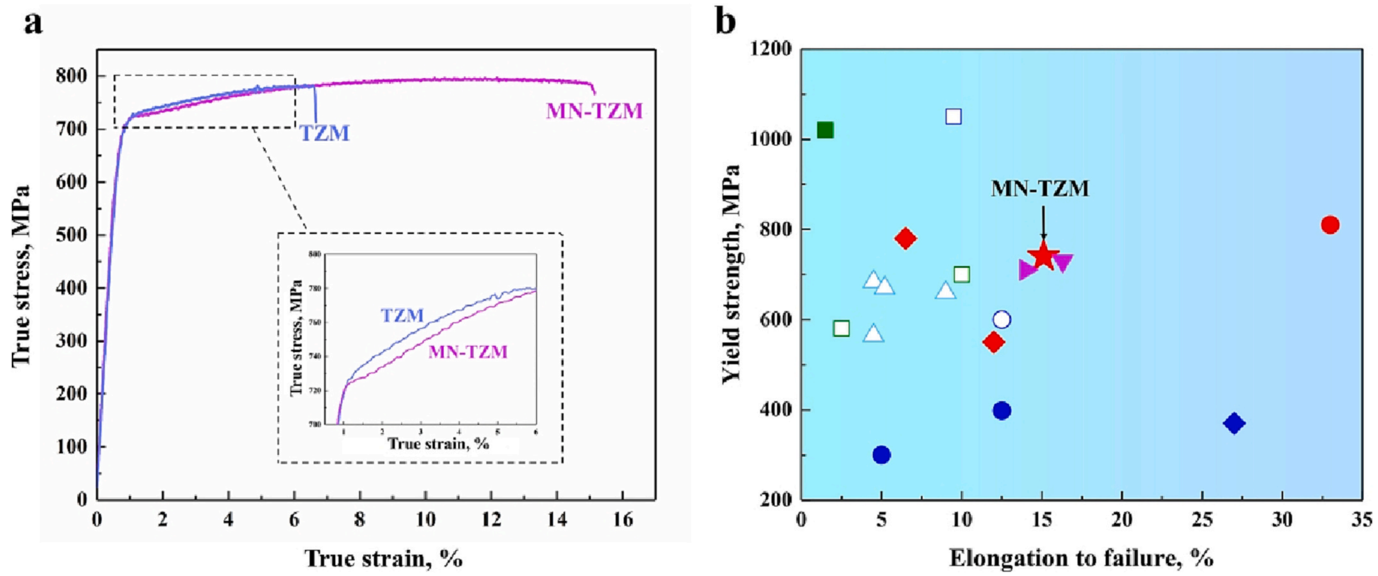

Fig. 6. (a) Room temperature true stress-strain tensile curves of the MN-TZM and TZM alloys, (b) Yield strength versus total tensile elongation of MN-TZM compared with literature data. The present MN-TZM data are shown as a red-filled star. The literature data are for representative Mo alloys, including CP-Mo (filled blue circles) [37], Mo—Re (open blue circle) [38], ODS-Mo (open light blue triangles) [38], LCAC-Mo (open green squares) [39], TZM (filled red diamonds) [40], HIP-TZM (hot isostatic pressing) (filled green squares) [40], SPS-TZM (spark plasma sintering) (open blue square) [40], ODS-Mo-Re (open bule diamond) [41], APM-TZM (arc melting process) (filled purple down triangle) [39], APM-ODS-Mo (filled purple right triangle) [39], NS-Mo (nanostructure) (filled red circle) [12]. (For interpretation of the references to colour in this figure legend, the reader is referred to the web version of this article.)

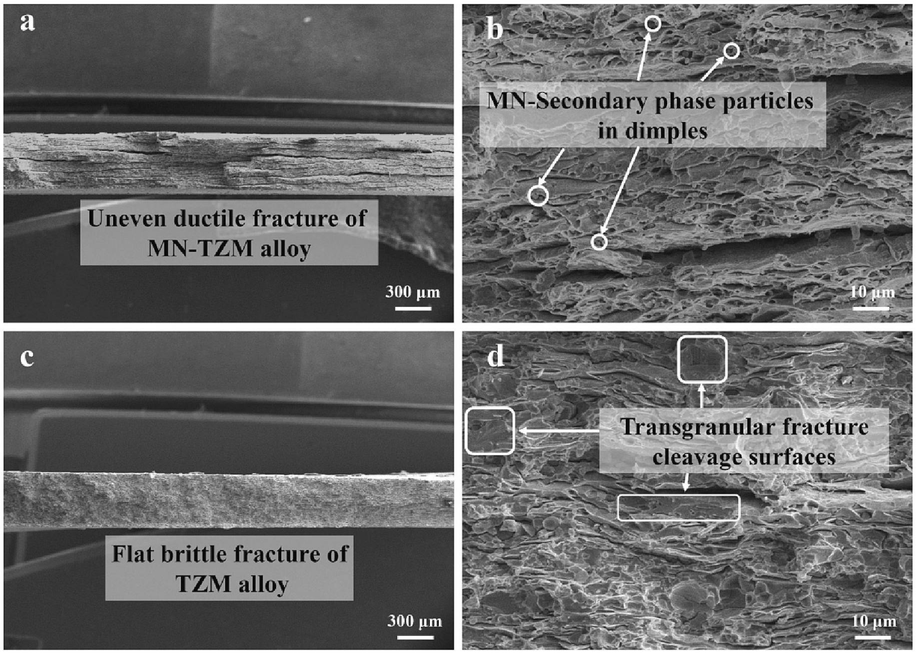

Fig. 7. Room temperature tensile fracture surfaces of Mo alloys: (a), (b) MN-TZM alloy; (c), (d) TZM alloy.

size of the studied annealed MN-TZM alloy sheets are smaller than the TZM alloy. From Eqs. (4), (5), and (7), TZM alloys are more prone to brittle fracture.

In addition, if the identical secondary phase particles are uniformly dispersed in the matrix, the effect of crack nucleation will be significantly reduced. However, with the growth of the secondary phase particle, the effect of crack nucleation increases gradually, which is closely related to the shape of the secondary phase. When the elastic strain energy of the particles reaches the surface formation energy under load, the interface will generate a new surface by releasing the strain energy. The corresponding energy can be expressed as [36]:

$$\eta\sigma = \left(E\gamma/_{d}\right)^{1/2} \tag{8}$$

Here, σ is the applied stress, η is the stress concentration factor, γ is the interface fracture energy, E is the elastic modulus, and d is the particle diameter of the secondary phase. It can be seen from Eq. (8) that the larger the particle size of the secondary phase in the alloy, the easier it is for cracks to nucleate.

From Fig. 3c, d, the MN-SP particles of the MN-TZM alloy maintain a spherical shape after rolling. The M-SP particles in the TZM alloy are destroyed and exhibit an irregular shape due to the large load area. It can be concluded from Fig. 8 that when the dislocations are packed around the secondary phase, the fine spherical particles of the secondary phase are equivalent to microscopic pores, which promotes ductile fracture of the material. Irregular, fractured, large-scale secondary phases are equivalent to microcracks, which contribute to brittle fracture in the material.

3.5. Deformation mechanism of the MN-TZM alloy

3.5.1. Stacking fault energy analysis

EBSD and TEM characterization of the tensile specimens tested to different maximum strain was performed to investigate the deformation mechanism of the two Mo alloys at room temperature. As seen in Fig. 9a, b, corrugated slip bands (yellow curves) were found in the MN-TZM alloy at 3% strain. This is considered a cross-slip of screw dislocations and dislocation tangle (TG). Studying the stacking fault energy of materials helps reveal the slip process of dislocations. Stacking fault energy usually refers to stable stacking fault energy. Scholars have used various methods to study the stable stacking fault energy, including experiments [45] and theoretical calculations [46]. However, some scholars [47] pointed out that the stable stacking fault energy alone cannot explain the dislocation nucleation mechanism.

Generalized stacking fault energy (γ_{GSF} plane) includes stable stacking fault energy and unstable stacking fault energy, which can better reflect the slip properties of metal crystals. The generalized stacking fault energy refers to the energy difference per unit area in the stacking fault process of the two structures constituting the supercell along the slip vector u from $u = 0$ to $u \neq 0$. The maximum value on the γ_{GSF} plane is the unstable stacking fault energy γ_{us}, which not only plays a key role in the structure of the dislocation nucleation point but also determines the difficulty of the slip process. The larger the γ_{us} is, the more complex the slip of dislocations is, and the more difficult it is for the material to undergo shear deformation. Hao [48] et al. used the first principles based on density functional theory to calculate the generalized stacking fault energy when compressive and tensile stresses were applied to the bcc Mo metal. Due to the periodic arrangement of crystals, the generalized stacking fault surface energy γ(u) satisfies the following symmetry transformation:

$$\gamma(R+u)=\gamma(u) \tag{9}$$

Here, R is the lattice basis vector, and u is the slip displacement. Hao [48] calculated the generalized stacking fault surface energy on the Mo {110} surface by first principles based on the density functional theory and concluded that $\langle 111\rangle\{110\}$ is the most slippery system in the Mo metal system. Calculations show that γ_{us} appears at $u = 0.5b$ during tension. As the tensile stress increases, the γ_{us} in the [110] direction gradually decreases. The greater the tensile stress applied to Mo, the more significant the reduction of γ_{us}. This indicates that the shear deformation of the slip system within the material will easily occur after tensile stress is applied in the [110] direction of Mo. Table 2 lists the variation of γ_{us} with stress when Mo is subjected to tensile stress in the [110] and $[1\bar{1}1]$ directions. Different from the [110] direction, applying tensile stress in the $[1\bar{1}1]$ direction increases the value of γ_{us}. To sum up, for Mo, the direction of applying tensile stress perpendicular to the slip plane will cause Mo to undergo shear deformation easily, thus making the material brittle. When the applied tensile stress direction is parallel to the slip plane, the shear deformation of Mo is difficult to occur, thereby improving the toughness of the material.

It can be seen from Fig. 9d and h that the MN-TZM alloy contains MN-SP, so the slip of dislocations is less hindered by a single secondary phase. Dislocations in MN-TZM alloys can even slip through the MN-SP without changing the original slip direction. The slip directions of dislocations in MN-TZM alloys are closer to Mo and proceed along the (110) direction. Because of this, the γ_{us} in the (110) direction gradually decreases during tension of the MN-TZM alloy. This facilitates the slip of dislocations in the alloy, which ultimately improves the MN-TZM alloy plasticity. As can be seen from Fig. 9j and l that due to the presence of M-SP particles in the TZM alloy system, it is difficult for dislocations to cut through the secondary phase, so dislocations must change their slip directions. The slip of dislocations in the (301) direction increases the γ_{us} in this direction, eventually making the TZM alloy brittle.

In addition, during the deformation of MN-TZM alloy, the total dislocation is not easy to decompose due to the small hindrance effect of

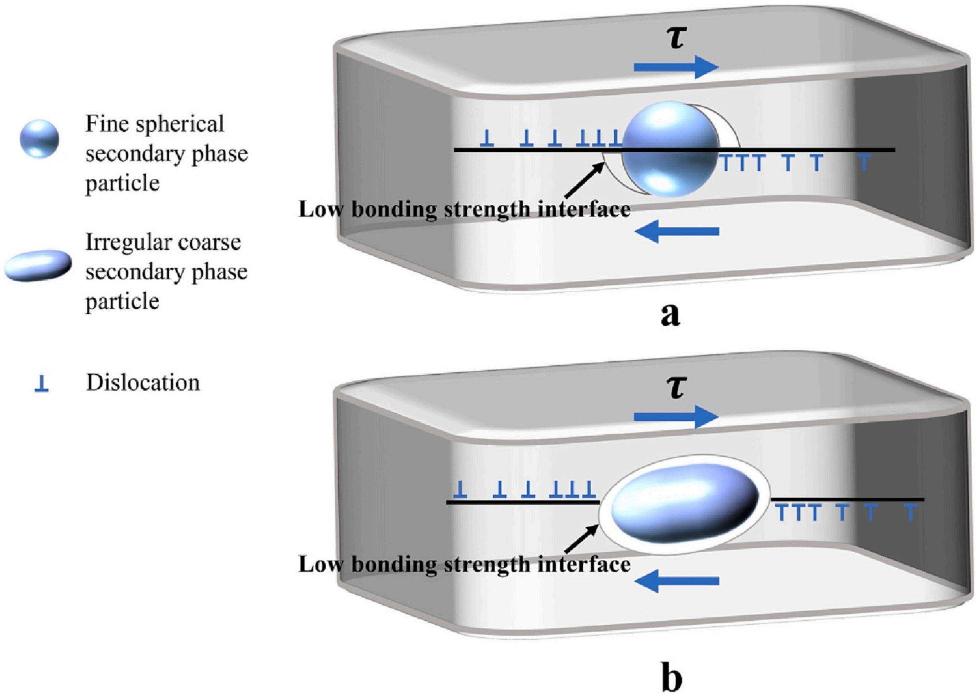

Fig. 8. Schematic diagram of the influence mechanism of secondary phase morphology on crack formation in Mo alloys: (a) Microscopic porosity effect of fine spherical secondary phase particles, (b) microcrack effect of irregular large-scale secondary phase particles.

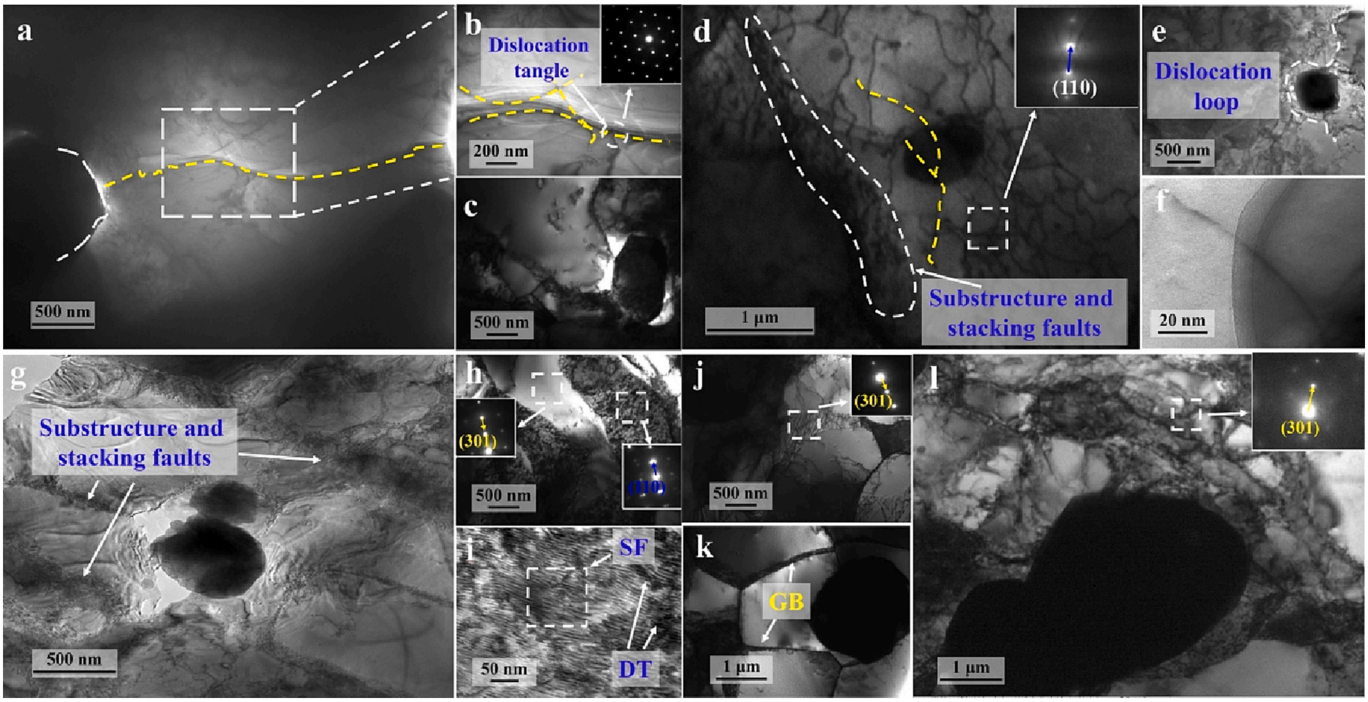

Fig. 9. TEM images of the studied Mo alloys deformed to different maximum strains: (a), (b), (c) MN-TZM at 3% strain, (d), (e), (f) MN-TZM at 9% strain, (g), (h), (i) MN-TZM 15.1% strain, (j) TZM 1.3% strain, (k) TZM 3.9%, strain and (l) TZM 6.6% strain.

Table 2
The unstable stacking fault energy (eV/Å^2) of Mo after applying tensile stress in the [110] and [1$\bar{1}$1] directions [48].

	0 GPa	1 GPa	3 GPa	5 GPa
[110]	0.10801	0.10601	0.10162	0.09708
[1$\bar{1}$1]	0.10801	0.10851	0.11306	0.11673

a single MN-SP on dislocation. When a dislocation encounters a MN-SP during slip, it can continue to move by cross-slipping or through the second phase until it meets other dislocations that are slipping to form a dislocation tangle (dislocation net), as shown in Fig. 9a, b, c, d, f, g, h, and i. Due to the existence of M-SP, TZM alloy is difficult to occur dislocation cross-slip, and the motion of the dislocation configuration is poor, as shown in Fig. 9j, k, and l.

3.5.2. Deformation mechanism

The EBSD analysis of the studied Mo alloys in the annealed state is shown in Fig. 5. Combined with Fig. 10, it can be found that the average grain size of the MN-TZM alloy in the annealed state is 1.43 ± 5.4 μm. When the strain is 9%, it is 1.82 ± 4.7 μm. The grain size increases with the strain, indicating that the deformation of the MN-TZM alloy at the initial deformation stage is dominated by the slip of dislocations within the grains. From Fig. 9d, e, and f, it can be seen that the dislocation is cutting through or bypassing the MN-SP. By comparing Fig. 5b and Fig. 10b, it can be seen that the KAM value in the MN-TZM alloy with 9% strain is slightly lower than that of the rolled sheet, indicating that the slip of dislocations in the alloy is not significantly hindered, and thus does not increase the dislocation density. The deformation will cause an increase in the ratio of grain boundaries at small angles in the alloy. By comparing Fig. 5c and Fig. 10c, it can be seen that with the increase of strain, the ratio of small angle grain boundaries in MN-TZM alloy decreases by 17%. This shows that although the strain of MN-TZM alloy reaches 9% at this stage, the slip of dislocation inside the grain is not significantly hindered, which makes the grain of MN-TZM alloy gradually increase with the stretching so that the large angle grain boundary ratio increase. By comparing Fig. 5d and Fig. 10d, it can be seen that the substructure region of MN-TZM alloy has increased significantly, accompanied by a significant decrease in the deformation region. This shows that in the process of increasing the strain of MN-TZM alloy to 9%, the deformation mechanism of the alloy is the value-added of the substructure within the grain. In summary, the dislocations in the MN-TZM alloy are easy to slip over or bypass the MN-SP, thus avoiding premature saturation of the dislocation density. This process is the main reason the plasticity of MN-TZM alloy increases by 2.3 times without losing strength. As the strain increased to 15.1%, the grain size decreased to 1.59 ± 4.7 μm. At this time, the MN-TZM alloy contains more low-angle grain boundaries and larger KAM, and dislocation stacking faults and dislocation junctions within the substructure continue accumulating (as seen in Fig. 9g, h, and i). The strain continued to increase, and the substructure density in the MN-TZM alloy system reached a critical value to generate finer sub-grains. At the same time, the original grains were broken, eventually leading to material failure.

It can be seen from Fig. 5 and Fig. 11 that strain-induced grain refinement occurs in the TZM alloy during deformation. However, the high-angle and low-angle grain boundaries remain almost unchanged during the entire deformation process, and the sub-structure does not increase much at the later deformation stage. It shows that in the initial stage of the TZM alloy tensile deformation, dislocations cannot cut or bypass M-SP particles, and the dislocation density increases too fast, resulting in the rapid saturation of dislocation density in the TZM alloy, resulting in stress concentration. The dislocations cannot be transmitted smoothly and effectively between grains, resulting in the maximum strain of only 6.6% in the TZM alloy.

4. Conclusions

In this study, MN-TZM alloys containing MN-SP were prepared using titanium sulfate, zirconium nitrate, and fructose as raw materials. The microstructure, tensile properties, and deformation behavior of MN-TZM alloys were investigated. The main conclusions can be summarized as follows:

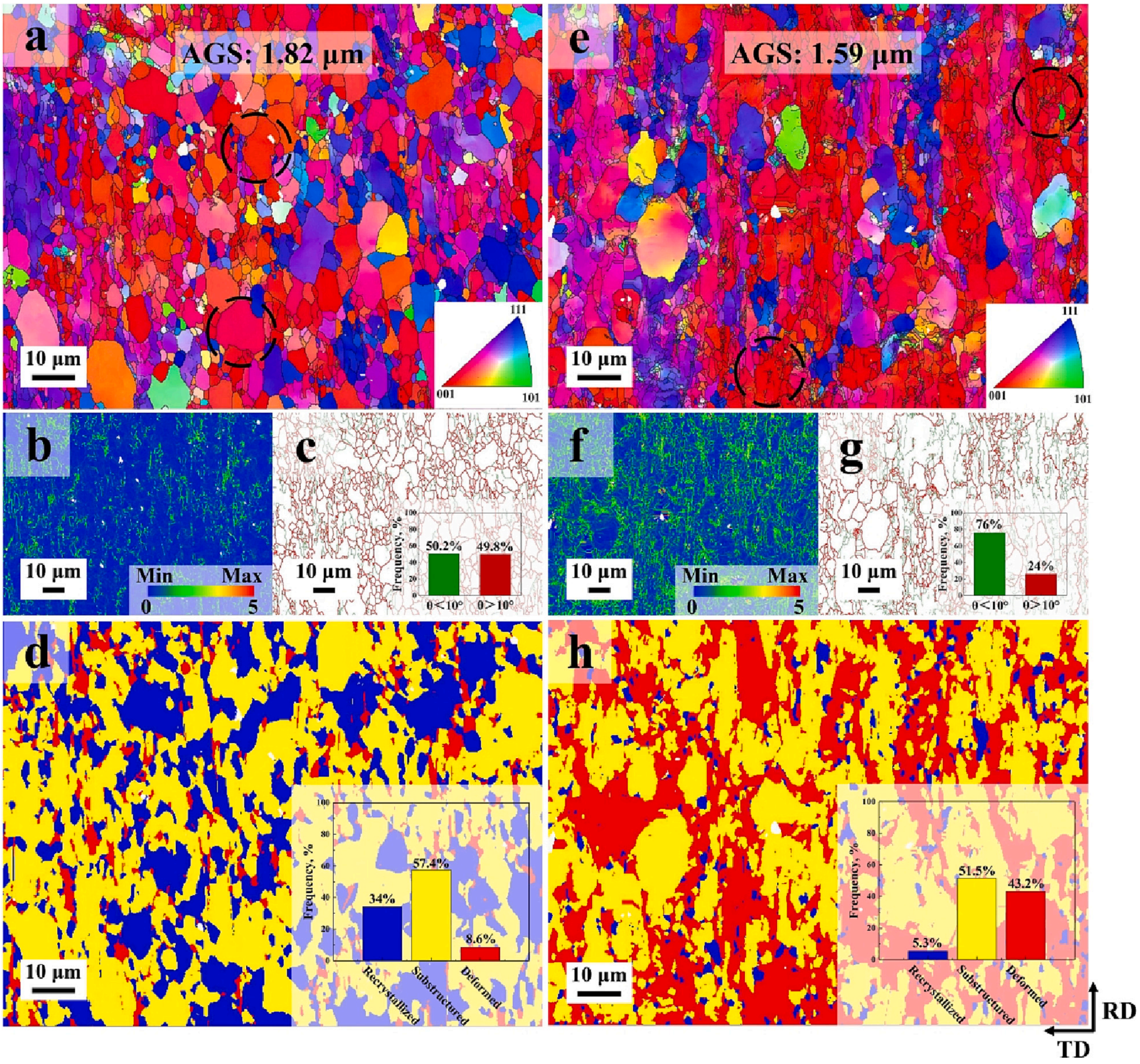

Fig. 10. IPF, KAM, grain boundary, recrystallized, sub-structured, and deformed composition diagrams of the MN-TZM alloy: (a), (b), (c), and (d) 9% strain, (e), (f), (g), and (h) 15.1% strain.

1) The room temperature elongation of the MN-TZM alloy is 2.3 times larger than the TZM alloy without loss of strength, reaching 15.1%. The fracture of MN-TZM alloy exhibits cleavage and ductile tear characteristics, which is a mixture of cleavage and quasi-cleavage fracture.
2) The MN-SP is uniformly distributed in the matrix, which has a stronger hindering effect on both volume diffusion (lattice diffusion) and grain boundary diffusion during the sintering process than M-SP.
3) The average grain size of the MN-TZM alloy sintered billet is reduced by 29.7% compared with the TZM alloy. The MN-SP hinders the grain boundary expansion during the recrystallization of Mo alloys more strongly than M-SP. Therefore, the average grain size of the annealed MN-TZM alloy is 24.3% lower than the TZM alloy.
4) The dislocations generated when the MN-TZM alloy is stretched can easily slip around or through the MN-SP along the (110) direction. Stacking faults and dislocation junctions in the MN-TZM alloy substructure avoid stress concentrations.

CRediT authorship contribution statement

Shi-Lei Li: Data curation, Validation, Investigation, Methodology, Software, Writing – original draft, Writing – review & editing. **Ping Hu:** Writing – review & editing, Supervision, Resources. **Tong Liu:** Data curation, Investigation. **Qian-Shuang Shi:** Data curation, Validation, Investigation. **Bo-Liang Hu:** Investigation, Visualization, Resources. **Xing-Jiang Hua:** Investigation. **Song-Wei Ge:** Supervision, Investigation. **Jia-Yu Han:** Formal analysis, Visualization. **Wen Zhang:** Writing – review & editing, Supervision. **Kuai-She Wang:** Writing – review & editing, Supervision. **Alex A. Volinsky:** Writing – review & editing.

Declaration of Competing Interest

The authors declare that they have no known competing financial interests or personal relationships that could have appeared to influence the work reported in this paper.

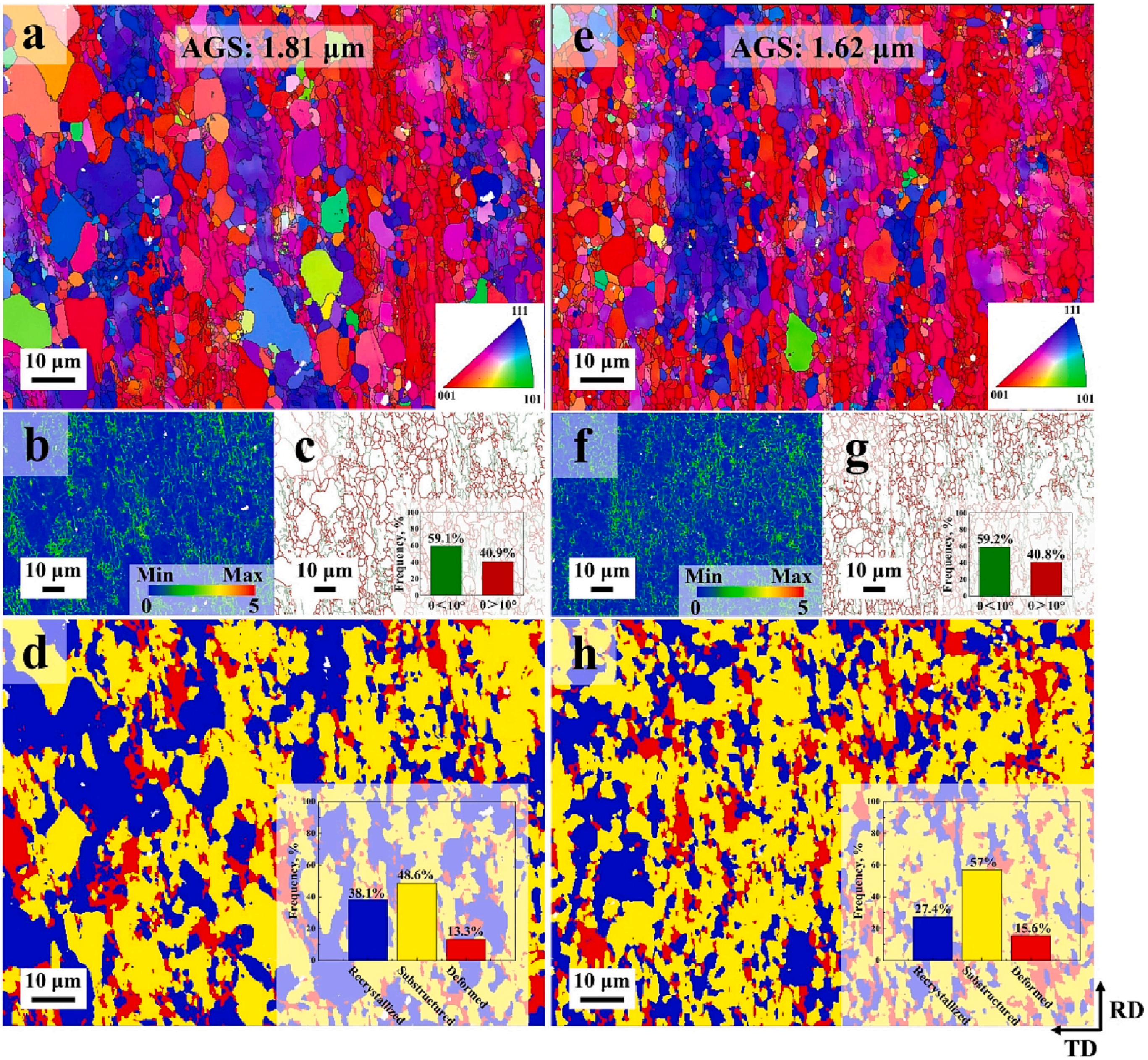

Fig. 11. IPF, KAM, grain boundary, recrystallized, sub-structured, and deformed composition diagram of the TZM alloy: (a), (b), (c), and (d) 3.9% strain, (e), (f), (g), and (h) 6.6% strain.

Data availability

The raw/processed data required to reproduce these findings cannot be shared at this time due to legal or ethical reasons.

Acknowledgments

This work was supported by the Scientific and Technological Innovation Team Project of the Shaanxi Innovation Capability Support Plan, China (2022TD-30), Key R&D Program of the Shaanxi Province, China (2021GY-209), Service Local Special Program of Education Department of the Shaanxi province (21JC016), the Fok Ying Tung Education Foundation (171101), the Youth Innovation Team of the Shaanxi Universities (2019-2022), General Special Scientific Research Program of the Shaanxi Provincial Department of Education (21JK0722), Top Young Talents Project "Special Support Program for High-level Talents" in the Shaanxi Province (2018-2023), National Natural Science Foundation of China (52104382), Major Special Projects of Science and Technology in the Shanxi Province (20191102006), the China Postdoctoral Science Foundation (2021M693878) and International Science and Technology Cooperation Program of the Shaanxi Province (2022KW-39).

References

[1] L. Lu, Y.F. Shen, X.H. Chen, L.H. Qian, K. Lu, Ultrahigh strength and high electrical conductivity in copper, Science 304 (2004) 422–426, https://doi.org/10.1126/science.1092905.

[2] X.Y. Li, Y.J. Wei, L. Lu, K. Lu, H.J. Gao, Dislocation nucleation governed softening and maximum strength in nano-twinned metals, Nature 464 (2010) 877–880, https://doi.org/10.1038/nature08929.

[3] J.J. Ni, J. Li, W. Luo, Q. Han, Y.B. Yin, Z.F. Jia, B.X. Huang, C.C. Hu, Z.L. Xu, Microstructure and properties of in-situ TiC reinforced copper nanocomposites fabricated via long-term ball milling and hot pressing, J. Alloys Compd. 755 (2018) 24–28, https://doi.org/10.1016/j.jallcom.2018.04.327.

[4] Z. Dong, Z.Q. Ma, L.M. Yu, Y.C. Liu, Achieving high strength and ductility in ODS-W alloy by employing oxide@W core-shell nanopowder as precursor, Nat. Commun. 12 (2021), https://doi.org/10.1038/s41467-021-25283-2.

[5] Y.Q. Bu, Y. Wu, Z.F. Lei, X.Y. Yuan, H.H. Wu, X.B. Feng, J.B. Liu, J. Ding, Y. Lu, H. T. Wang, Z.P. Lu, W. Yang, Local chemical fluctuation mediated ductility in body-centered-cubic high-entropy alloys, Mater. Today 46 (2021) 28–34, https://doi.org/10.1016/j.mattod.2021.02.022.

[6] W.W. Sun, Y.M. Zhu, R. Marceau, L.Y. Wang, Q. Zhang, X. Gao, C. Hutchinson, Precipitation strengthening of aluminum alloys by room-temperature cyclic plasticity, Science 363 (2019) 972–975, https://doi.org/10.1126/science.aav7086.

[7] T.H. Fang, W.L. Li, N.R. Tao, K. Lu, Revealing extraordinary intrinsic tensile plasticity in gradient nano-grained copper, Science 331 (2011) 1587–1590, https://doi.org/10.1126/science.1200177.

[8] X. Zhou, X.Y. Li, K. Lu, Size dependence of grain boundary migration in metals under mechanical loading, Phys. Rev. Lett. 122 (2019), https://doi.org/10.1103/PhysRevLett.122.126101.

[9] X.C. Liu, H.W. Zhang, K. Lu, Strain-induced ultrahard and ultrastable nanolaminated structure in nickel, Science 342 (2013) 337–340, https://doi.org/10.1126/science.1242578.

[10] Y.K. Lee, J.E. Jin, Y.Q. Ma, Transformation-induced extraordinary ductility in an ultrafine-grained alloy with nanosized precipitates, Scr. Mater. 57 (2007) 707–710, https://doi.org/10.1016/j.scriptamat.2007.06.047.

[11] Y.N. Zan, Y.T. Zhou, Z.Y. Liu, G.N. Ma, D. Wang, Q.Z. Wang, W.G. Wang, B.L. Xiao, Z.Y. Ma, Enhancing strength and ductility synergy through heterogeneous structure design in nanoscale Al_2O_3 particulate reinforced Al composites, Mater. Des. 166 (2019), https://doi.org/10.1016/j.matdes.2019.107629.

[12] G. Liu, G.J. Zhang, F. Jiang, X.D. Ding, Y.J. Sun, J. Sun, E. Ma, Nanostructured high-strength molybdenum alloys with unprecedented tensile ductility, Nat. Mater. (2013) 344–350, https://doi.org/10.1038/nmat3544.

[13] M.A. Harimon, N.A. Hidayati, Y. Miyashita, Y. Otsuka, Y. Mutoh, S. Yamamoto, H. Aoyama, High temperature fracture toughness of TZM alloys with different kinds of grain boundary particles, Int. J. Refract. Met. Hard Mater. 66 (2017) 52–56, https://doi.org/10.1016/j.ijrmhm.2017.02.006.

[14] Z.B. Jiao, J.H. Luan, M.K. Miller, C.Y. Yu, C.T. Liu, Effects of Mn partitioning on nanoscale precipitation and mechanical properties of ferritic steels strengthened by NiAl nanoparticles, Acta Mater. 84 (2015) 283–291, https://doi.org/10.1016/j.actamat.2014.10.065.

[15] B.L. Hu, J.Y. Han, S.-W. Ge, X.J. Hua, S.L. Li, H.R. Xing, K.S. Wang, P. Hu, J.B. Fu, W. Zhang, A.A. Volinsky, E.S. Marchenko, Secondary phases strengthening-toughening effects in the Mo-TiC-La_2O_3 alloys, Mater. Sci. Eng. A 831 (2022), https://doi.org/10.1016/j.msea.2021.142271.

[16] B.V. Cockeram, The fracture toughness and toughening mechanism of commercially available unalloyed molybdenum and oxide dispersion strengthened molybdenum with an Equiaxed, large grain structure, Metall. Mater. Trans. A 40 (2009) 2843–2860, https://doi.org/10.1007/s11661-009-9919-9.

[17] M.S. El-Genk, J.M. Tournier, A review of refractory metal alloys and mechanically alloyed-oxide dispersion strengthened steels for space nuclear power systems, J. Nucl. Mater. 340 (2005) 93–112, https://doi.org/10.1016/j.jnucmat.2004.10.118.

[18] B.V. Cockeram, R.W. Smith, N. Hashimoto, L.L. Snead, The swelling, microstructure, and hardening of wrought LCAC, TZM, and ODS molybdenum following neutron irradiation, J. Nucl. Mater. 418 (2011) 121–136, https://doi.org/10.1016/j.jnucmat.2011.05.055.

[19] T.S. Byun, M. Li, B.V. Cockeram, L.L. Snead, Deformation and fracture properties in neutron irradiated pure Mo and Mo alloys, J. Nucl. Mater. 376 (2008) 240–246, https://doi.org/10.1016/j.jnucmat.2008.03.004.

[20] B.L. Hu, K.S. Wang, P. Hu, Y.H. Zhou, J. Deng, W.J. Chen, P.F. Feng, J.P. Zhang, A. A. Volinsky, H.L. Yu, Secondary phases formation in lanthanum-doped titanium-zirconium-molybdenum alloy, J. Alloys Compd. 757 (2018) 340–347, https://doi.org/10.1016/j.jallcom.2018.05.103.

[21] B. Dubiel, M. Chmielewski, T. Moskalewicz, A. Gruszczynski, A. Czyrska-Filemonowicz, Microstructural characterization of novel Mo-Re-Al_2O_3 composite, Mater. Lett. 124 (2014) 137–140, https://doi.org/10.1016/j.matlet.2014.02.098.

[22] L.J. Xu, S.Z. Wei, D.D. Zhang, Y. Li, G.S. Zhang, J.W. Li, Fine structure and interface characteristic of α-Al_2O_3 in molybdenum alloy, Int. J. Refract. Met. Hard Mater. 41 (2013) 483–488, https://doi.org/10.1016/j.ijrmhm.2013.06.006.

[23] L.A. Diaz, A.F. Valdes, C. Diaz, A.M. Espino, R. Torrecillas, Alumina/molybdenum nanocomposites obtained in organic media, J. Eur. Ceram. Soc. 23 (2003) 2829–2834, https://doi.org/10.1016/s0955-2219(03)00295-4.

[24] L.J. Xu, S.Z. Wei, J.W. Li, G.S. Zhang, B.Z. Dai, Preparation, microstructure and properties of molybdenum alloys reinforced by in-situ Al_2O_3 particles, Int. J. Refract. Met. Hard Mater. 30 (2012) 208–212, https://doi.org/10.1016/j.ijrmhm.2011.08.012.

[25] I.M. Gunter, J.H. Schneibel, J.J. Kruzic, Ductility and fracture toughness of molybdenum with $MgAl_2O_4$ additions, Mater. Sci. Eng. A 458 (2007) 275–280, https://doi.org/10.1016/j.msea.2006.12.128.

[26] P. Hu, F. Yang, J. Deng, T. Chang, B.L. Hu, J.F. Tan, K.S. Wang, W.C. Cao, P. F. Feng, H.L. Yu, High temperature mechanical properties of TZM alloys under different lanthanum doping treatments, J. Alloys Compd. 711 (2017) 64–70, https://doi.org/10.1016/j.jallcom.2017.03.346.

[27] P. Hu, F. Yang, K.S. Wang, Z.T. Yu, J.F. Tan, R. Song, B.L. Hu, H. Wang, H.C. He, A. A. Volinsky, Preparation and ductile-to-brittle transition temperature of the La-TZM alloy plates, Int. J. Refract. Met. Hard Mater. 52 (2015) 131–136, https://doi.org/10.1016/j.ijrmhm.2015.05.006.

[28] K.S. Wang, J.F. Tan, P. Hu, Z.T. Yu, F. Yang, B.L. Hu, R. Song, H.C. He, A. A. Volinsky, La_2O_3 effects on TZM alloy recovery, recrystallization and mechanical properties, Mater. Sci. Eng. A 636 (2015) 415–420, https://doi.org/10.1016/j.msea.2015.03.114.

[29] P.N. Browning, J. Fignar, A. Kulkarni, J. Singh, Sintering behavior and mechanical properties of Mo-TZM alloyed with nanotitanium carbide, Int. J. Refract. Met. Hard Mater. 62 (2017) 78–84, https://doi.org/10.1016/j.ijrmhm.2016.10.002.

[30] T. Mrotzek, A. Hoffmann, U. Martin, Hardening mechanisms and recrystallization behaviour of several molybdenum alloys, Int. J. Refract. Met. Hard Mater. 24 (2006) 298–305, https://doi.org/10.1016/j.ijrmhm.2005.10.003.

[31] W.X. Song, Metals, Metallurgical Industry Press, 1989.

[32] G.X. Hu, X. Ca, Y.H. Rong, Fundamentals of Material Science, ShangHai JiaoTong University Press, 2006.

[33] P.Y. Huang, Principle of Powder Metallurgy, Metallurgical Industry Press, 1995.

[34] S.L. Li, P. Hu, Y.G. Zuo, H.R. Xing, J.Y. Han, S.W. Ge, X.J. Hua, B.L. Hu, C.J. Cui, K. S. Wang, Precise control of oxygen for titanium-zirconium-molybdenum alloy, Int. J. Refract. Met. Hard Mater. 103 (2022), 105768, https://doi.org/10.1016/j.ijrmhm.2021.105768.

[35] Y.V.R.K. Prasad, K.P. Rao, S. Sasidhara, Hot Working Guide: Compendium of Processing Maps, 2015.

[36] P. Hu, Y.H. Zhou, J. Deng, S.J. Li, W.J. Chen, T. Chang, B.L. Hu, K.S. Wang, P. F. Feng, A.A. Volinsky, Crack initiation mechanism in lanthanum-doped titanium-zirconium-molybdenum alloy during sintering and rolling, J. Alloys Compd. 745 (2018) 532–537, https://doi.org/10.1016/j.jallcom.2018.02.191.

[37] D. Sturm, M. Heilmaier, J.H. Schneibel, P. Jéhanno, B. Skrotzki, H. Saage, The influence of silicon on the strength and fracture toughness of molybdenum, Mater. Sci. Eng. A 463 (2007) 107–114, https://doi.org/10.1016/j.msea.2006.07.153.

[38] A.J. Mueller, R. Bianco, R.W. Buckman, Evaluation of oxide dispersion strengthened (ODS) molybdenum and molybdenum–rhenium alloys, Int. J. Refract. Met. Hard Mater. 18 (2000) 205–211, https://doi.org/10.1016/S0263-4368(00)00028-7.

[39] B.V. Cockeram, The mechanical properties and fracture mechanisms of wrought low carbon arc cast (LCAC), molybdenum–0.5pct titanium–0.1pct zirconium (TZM), and oxide dispersion strengthened (ODS) molybdenum flat products, Mater. Sci. Eng. A 418 (2006) 120–136, https://doi.org/10.1016/j.msea.2005.11.030.

[40] T. Takida, H. Kurishita, M. Mabuchi, T. Igarashi, Y. Doi, T. Nagae, Mechanical properties of fine-grained, sintered molybdenum alloys with dispersed particles developed by mechanical alloying, Mater. Trans. 45 (2004) 143–148, https://doi.org/10.2320/matertrans.45.143.

[41] G.J. Zhang, Y.J. Sun, R.M. Niu, J. Sun, J.F. Wei, B.H. Zhao, L.X. Yang, Microstructure and strengthening mechanism of oxide lanthanum dispersion strengthened molybdenum alloy, Adv. Eng. Mater. 6 (2004) 943–948, https://doi.org/10.1002/adem.200400072.

[42] G.A. Sargent, M.K. Keshavan, H. Conrad, Dislocation Modelling of Physical Systems, Pergamon, 1981.

[43] A.H. Cottrell, Theory of dislocations, Prog. Met. Phys. 4 (1953) 205–264, https://doi.org/10.1016/0502-8205(53)90018-5.

[44] Q.P. Zhong, Z.H. Zhao, Fractures, Higher Education Press, 2006.

[45] X.W. Zhou, C. Nowak, R.S. Skelton, M.E. Foster, J.A. Ronevich, C. San Marchi, R. B. Sills, An Fe–Ni–Cr–H interatomic potential and predictions of hydrogen-affected stacking fault energies in austenitic stainless steels, Int. J. Hydrog. Energy 47 (2022) 651–665, https://doi.org/10.1016/j.ijhydene.2021.09.261.

[46] D. Wen, M.S. Titus, First-principles study of Suzuki segregation at stacking faults in disordered face-centered cubic Co-Ni alloys, Acta Mater. 221 (2021), 117358, https://doi.org/10.1016/j.actamat.2021.117358.

[47] D. Wolf, V. Yamakov, S.R. Phillpot, A. Mukherjee, H. Gleiter, Deformation of nanocrystalline materials by molecular-dynamics simulation: relationship to experiments, Acta Mater. 53 (2005) 1–40, https://doi.org/10.1016/j.actamat.2004.08.045.

[48] H.L. Yao, L.R. Ping, Z.W. Tong, B.H. Fang, D.M. Yun, Y. Zhi, X.L. Chun, L.X. Yan, First-principles study of mechanical properties of BCC metals tungsten and molybdenum under high pressure, Journal of Sichuan University(Natural Science Edition) 45 (2018) 1041–1048, https://doi.org/10.3969/j.issn.0490-6756.2018.05.022.